Chapter 7

EXAFS Study of RTA Effect on the Atomic Structure of InGaAsSbN Alloy

7.1 Extended X-ray Absorption Fine Structure (EXAFS)

The advent of synchrotron radiation sources has led to an impressive progress in almost all x-ray techniques. The phenomenon of EXAFS – Extended X-ray Absorption Fine Structure – has been known for about 70 years, and the basic physical explanation was provided by Kronig [99]. However, during the following several decades, a great deal of confusion still existed over the question of whether a long-range order theory formulated in terms of Bloch waves or a short-range order theory in terns of scattering by neighboring atoms [100–102] is more appropriate. A major source of the confusion was that quantitative comparisons between theory and experiment were nonexistent. At the end of 1970's, a dramatic improvement in the theoretical understanding of EXAFS occurred. It is now established that a single scattering short-range order theory is adequate under most circumstances. Presently, as far as absorption spectroscopy is concerned, it has become possible to exploit the fine structure of the absorption coefficient to get information on both the geometric and electronic local structure of matter [103–105].

The origin of extended X-ray Absorption Fine Structure (EXAFS) is easily understood on purely phenomenological grounds. When an X-ray photon of high enough energy is absorbed by an atom, a core electron is ejected from the atom. The kinetic energy of the photoelectron is the difference between the photon's energy and the core binding energy. The outgoing photoelectron is described by a spherical wave, whose wavelength decreases when the photon energy increases. If the absorber atom is not isolated, the photoelectron can be backscattered by neighboring atoms, giving rise to an incoming spherical wave (Fig. 7.1). The absorption coefficient μ depends, to first order, on the dipole matrix element between the initial core state and the photoelectron's final state, which in turn is a superposition of the outgoing and incoming spherical waves. The phase relationship between outgoing and incoming waves depends on the photoelectron wavelength and the interatomic distance R. The variation of this phase relationship as a function of photon energy influences the final state amplitude at the core site, giving rise to an interference phenomenon which modulates the absorption coefficient. The frequency of EXAFS oscillations depends on the distance between ab-

sorber and back-scatterer atoms. Their amplitude is proportional to the number of back-scatterer atoms.

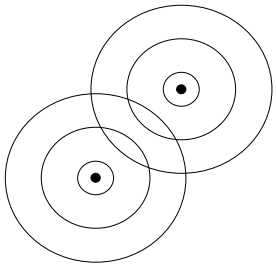

Figure 7.1: Outgoing photo electron waves propagate to neighboring atoms. The back-scattered waves modify the wave function at the central atom and give rise to EXAFS.

If we take the one electron approximation, i.e., in the absorption atom, only one core electron changes its state (and the electric-dipole approximation, which is applicable when the wavelength is much larger than the extension of the system), and the sudden approximation; i.e., when the photoelectron energy is relatively high, its interaction with the other electrons besides the core electron can be neglected, and finally a weak disorder (including thermal disorder and structural disorder), we can obtain a formula for the absorption coefficient:

$$\chi(k,T) = (S_0^2/k) N_{degen} \left| f(k) \right| (e^{-C_1 k/\pi}/C_1^2) \times e^{-2k^2 C_2} sin\left[2kC_1 + \phi(k)\right] \tag{7.1}$$

In equation 7.1, S_0^2 is the fraction of total absorption giving rise to elastic excitations, N_{degen} is the coordination number (number of nearest-neighbor atoms), C_1 is the average interatomic distance, C_2 corresponds to the mean-square relative displacement of the absorber and back-scatterer atoms, the exponential $e^{-2k^2C_2}$ is called the EXAFS Debye-Waller factor, $|f(k)|$ is the magnitude of the electron scattering factor, and $\phi(k)$ is the phase shift of the photoelectron caused by the potential of the back scattering atom.

Since the early development of X-ray absorption spectroscopy, it has been recognized that this technique could provide valuable information on the local geometric arrangement of dopants and defects in semiconductors [106]. Up to now, the analysis of the EXAFS has been used to determine the coordination of a number of dopants in semiconductors [107–111].

7.2 Sample Growth and Post-Growth Treatment

The samples were grown by solid-source molecular beam epitaxy on semi-insulating GaAs (100) substrates. The growth chamber was equipped with a radio frequency plasma cell as the N source. Growth temperature for the quantum wells was 410°C. The samples consist of multi-quantum-well structures (3 repetitions) of thickness 8 nm

separated by 15 nm of GaAs and covered by a GaAs cap 50 nm thick. The concentration of In was 38%.

Annealing was performed at 800°C. The as-grown samples (A0) and samples after anneal of 15 s (R15) and 60 s (A3) were studied in this work.

7.3 Experimental Setup

The experiments were conducted at the BM 29 beam line of the European Synchrotron Radiation Facility (ESRF) with a fluorescence measurement setup.

The beamline spectrometer used for the experiments is built within the downstream tangential fan from a hard bending magnet of this third-generation synchrotron radiation source. The experimental setup relevant to the optical design includes (as shown in Fig. 7.2):

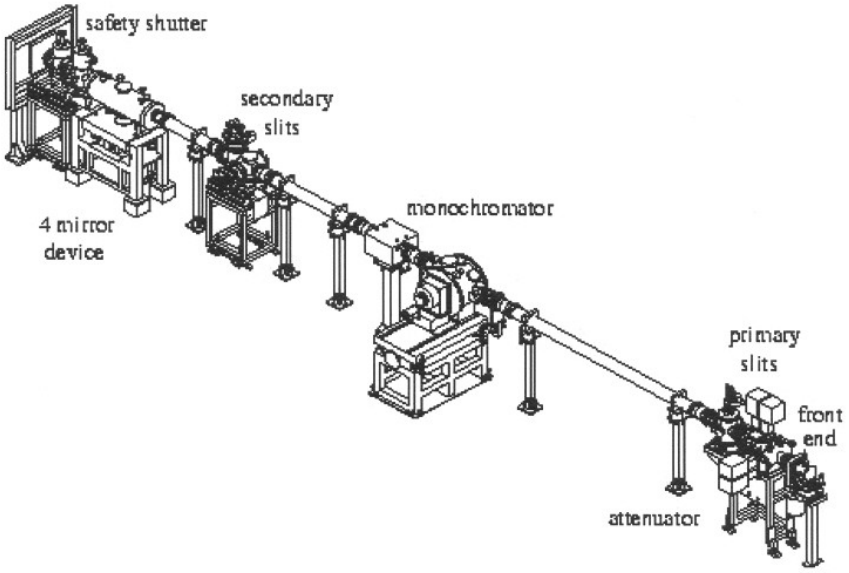

Figure 7.2: Components of the BM29 optics hutch.

1. Front end shutter and Be window

   To protect the machine front end from vacuum failures and to facilitate operation, the beam line is equipped with a thick Be window following the front end shutter.

2. Primary slits

   The slits are used to define the white-beam profile that is incident on the monochromator crystals. The primary slits vertical aperture is a particularly important parameter, as it largely defines the energy resolution of the instrument for a given set of monochromator crystals.

3. Monochromator

   The monochromator is a double crystal, fixed-exit double cam type from Kohzu-Seiki Corporation, Japan. Its operating geometry is in the vertical plane with the first crystal mounted so as to be able to rotate and translate along a mechanical cam, directing the Bragg reflected beam upwards. The second crystal in the monochromator is free to rotate about a single axis, and thus in combination with the translation and rotation of the first crystal, it Bragg diffracts the beam through a fixed exit point – parallel with the horizontal plane of the incident white beam. The monochromator crystal pair used in our experiment was Si (311), which is usable in the energy range of 5 keV to 50 keV.

4. Secondary slits

   Following the monochromator is the standard secondary slit package, installed to control the energy resolution and to eliminate possible parasitic reflections from the monochromator. In most operating modes these slits are used to define the horizontal beam profile,

5. Safety shutter

   This beam shutter isolates the experimental hutch from the monochromatic source. The shutter allows work to be performed at the experimental end stations of the beam line while beam is taken in the optics hutch.

6. Experimental slits

   An experimental slit package permits the accurate definition of the incident beam dimensions at the sample, and forms in combination with the secondary slits a tube spectrometer configuration.

7. Detectors

   We carried out fluorescence measurement on the InGaAsSbN samples. The In $K\alpha$ fluorescence was monitored using a thirteen element Ge hyperpure detector.

8. Cryostat

   We used a closed-cycle liquid nitrogen cryostat that operates in the 70 K to 450 K range for the EXAFS measurements. The samples were vertically attached in the holder. The incident beam and the fluorescence beam make an angle of 45^o with the sample surface.

The mirror package and attenuator are also part of the optical setup, but were not used in our EXAFS experiment.

7.4 Data Analysis

The analysis software is part of the UWXAFS package 20. These programs include AUTOBK21 for background removal, FEFF7 for generation of the theoretical models, and FEFFIT2 for parameter optimization of the model. A brief description of the analysis procedure used is given below:

7.4.1 Background Removal

Fig. 7.3. shows the absorption spectrum of sample R15:

$$\mu(E) \propto I_f / I_0 \tag{7.2}$$

In equation 7.2, I_f is the measured fluorescence intensity, and I_0 is the incident intensity. The modulations above the K edge near 11 keV are due to the EXAFS $\chi(k)$ from several shells of neighboring atoms adding together. The first step in the analysis is to isolate $\chi(k)$ from the total absorption coefficient $\mu(E)$.

$$\chi(E) = \frac{\mu(E) - \mu_0(E)}{\Delta\mu(E_0)} \tag{7.3}$$

In equation 7.3, $\chi(E)$ is the normalized oscillatory part of the absorption coefficient, $\mu(E)$ is the measured absorption coefficient: $\mu_0(E)$ is the background absorption coefficient, $\Delta\mu(E_0)$ is the value at the edge step E_0. Since the smooth absorption of an isolated atom $\mu_0(E)$ is not generally available experimentally and since present theoretical calculations of $\mu_0(E)$ are not sufficiently accurate for most EXAFS work ($\approx 0.01\%$), it is assumed that the smooth part of $\mu(E)$ represent the desired $\mu_0(E)$. Under this assumption, the remaining oscillatory part of $\mu(E)$ is computed as $\Delta\mu = \mu(E) - \mu_0(E)$ to give the normalized absorption coefficient $\chi(E) = \mu(E)/\Delta\mu(E_0)$, where $\Delta\mu(E_0)$ is the evaluated intensity of the absorption background, as shown in Figure 7.3.

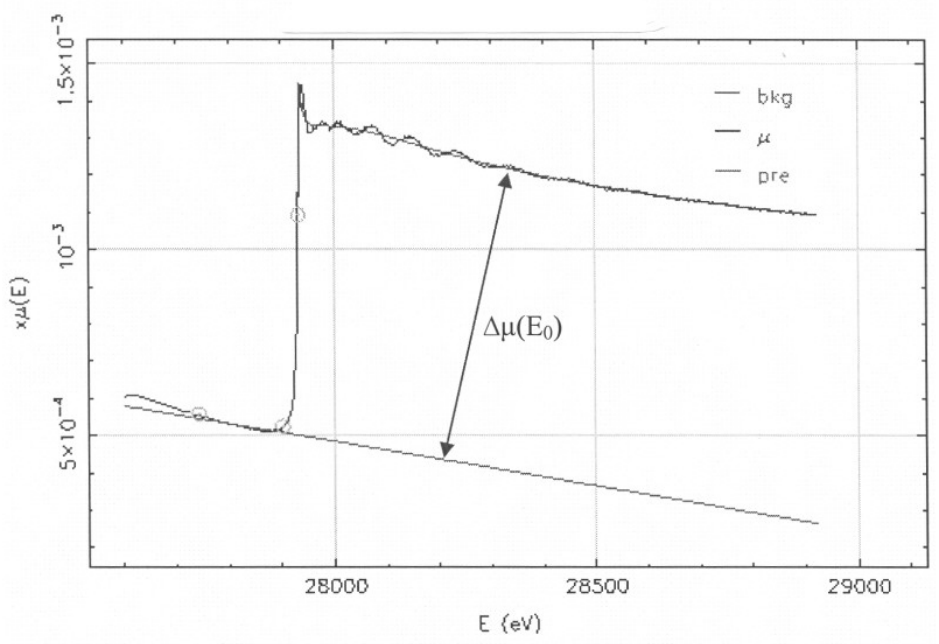

Figure 7.3: Experimental absorption signal, extrapolation of the pre-edge behavior and the evaluation of the atomic absorption coefficient.

One method for removing the background is to fit $\mu(E)$ (including the EXAFS) with polynomial splines or B spline [112, 113] using a least square procedure; a polynomial

spline or B spline is a function defined over a series of intervals with each interval containing a polynomial of some order. The ends or knots of the intervals are tied together so that the function and a specified number of derivatives are continuous across the knots. By specifying the number of intervals and the order of the polynomials, a very flexible function can be defined. A least squares fit with such a spline function enables the removal of low-frequency background components from $\mu(E)$ without affecting high frequency EXAFS signals. The R_{bkg} parameter determines the cutoff frequency below which the optimization occurs. Thus, the spline is varied until the transformed spectrum between 0 and R_{bkg} is optimized. In our analysis, R_{bkg} is set to 1.0 Å, 2 cubic splines were used to simulate the background.

The E_0 determination Since $\chi(k)$ in equation 7.1 is a function of k and not photon energy, k must be computed from experimental values of photon energies $\hbar\omega$, using

$$k = (2m/\hbar^2)^{1/2} \cdot (\hbar\omega - E_0)^{1/2} \tag{7.4}$$

There is no simple relation between features in the experimental spectrum and E_0 as defined by equation 7.4. In practice, E_0 is determined by the derivative maximum in the preedge range.

Fig. 7.4 shows the EXAFS modulation after converting from an E to a k scale and removing the smooth background using a polynomial spline fit. Figure 7.5 shows the curve that has been multiplied by k^2. The k^2 multiplication has the effect of weighting the EXAFS oscillations more uniformly over the range starting from about k=4 $Å^{-1}$. This step is important for preventing the larger amplitude oscillations from dominating the smaller ones in determining the interatomic distances, which depend only on frequency. Also, the k^2 weighting ensures that chemical effects on the EXAFS information, which are most significant at small k, are effectively cut off.

The window function that we used in the data analysis is also shown in Figs. 7.4 and 7.5. A window function is used to reduce the spurious oscillations induced by the finite k range. The window function can take a variety of functional forms, all of which arise from a small value (possibly zero) at low k, increase to one, and then fall back toward zero at high k. The window is intended to smooth out any ringing in the resulting FT amplitude while maintaining as much resolution as possible. In our data analysis, we chose a Kaiser-Bessel function.

7.4.2 Fourier Filtering

The direct transform from k to r space is :

$$F(r) = \int_{k_{min}}^{k_{max}} \chi(k) W(k) k^n exp(2ikr) dk \tag{7.5}$$

where W(k) is a window function. The integral limits k_{min} and k_{max} are chosen so as to exclude both the low k signal, where the EXAFS formula is unreliable, and the high k signal, where the signal-to-noise ratio is poor (n in equation (7.5) was chosen to be 2 in our study).

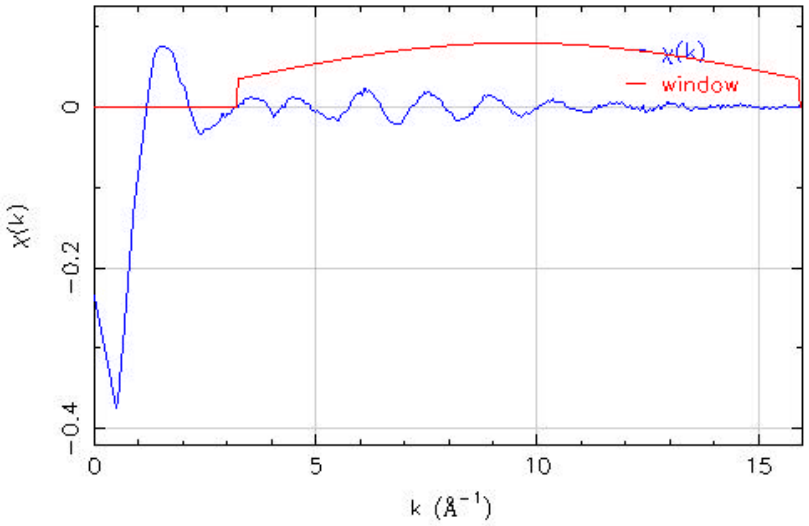

Figure 7.4: $\chi(k)$ derived from Fig. 7.3 by removing a smooth background using a polynomial spline fit. Photon energies have been converted to k values using equation 7.4.

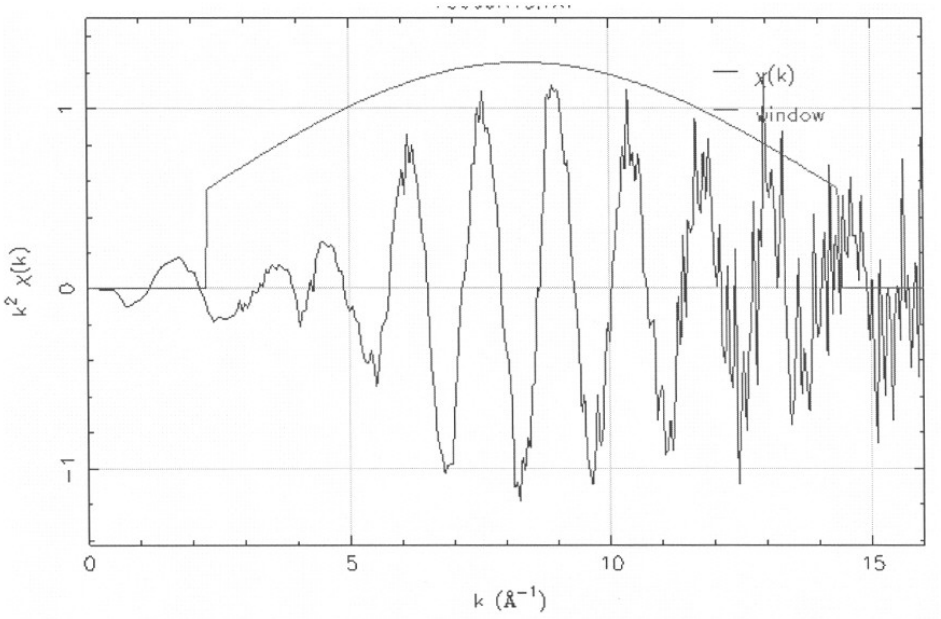

Figure 7.5: Data in Fig. 7.4 after multiplication by k^2. The multiplication roughly equalizes the amplitudes of the EXAFS oscillations.

Fig. 7.6 shows the magnitude of the Fourier transform of the data in Fig. 7.5. The curve was generated by first interpolating the non-uniformly spaced data onto a uniformly spaced k mash and then extending the data by adding to a range from k=0 $Å^{-1}$ to k=150 $Å^{-1}$. The extended data are then Fourier transformed using a fast Fourier

transformation algorithm.

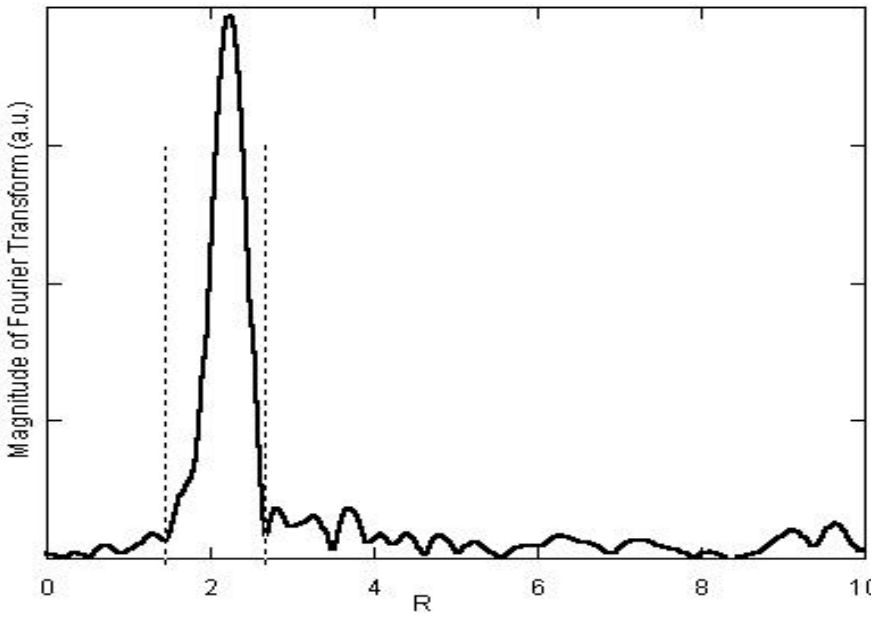

Figure 7.6: Fourier transform of the data in Figure 7.5.

In general, one prefers to isolate and separately analyze the contribution of each coordination shell through a procedure based on Fourier filtering, as shown in Fig. 7.6; here we set the R range for the analysis of the first shell in the spectrum.

Since the Fourier filtering introduces distortions, it is necessary that EXAFS spectra of reference samples as well as calculated EXAFS spectra undergo exactly the same filtering procedure as the experimental spectrum under analysis. The structural parameters can be obtained by simulating the EXAFS signal and optimizing its structural parameters by a best-fit to the experimental spectrum $\chi(k)$.

7.4.3 Goodness of Fit Value

When comparing 2 models, we used the Reduced chi-square (RCS) as a measure of the goodness of fit. The chi-square is defined as:

$$\chi^2 = \sum_{i=1}^{N} \left| \frac{X_{data} - X_{model}}{\epsilon_i} \right|^2 \tag{7.6}$$

In Equation 7.6, N is the number of function evaluations, and ϵ_i are the uncertainties in the function to minimize.

The reduced chi square is equal to chi square/k, where $k = N_{idp} - N_{var}$ is the number of degrees of freedom in the fit, (N_{idp} is the number of independent points, and N_{var} is the number of variables in the fit.

A decrease of the RCS value of 1 sigma error ($\sqrt{2/k}$) is regarded as the criterion of substantial improvement of the simulation result.

7.5 InGaAsSbN Sample EXAFS Data Analysis

7.5.1 Simulation

In the simulation, a theoretical model was built by giving a trial structure as input to the FEFF7 code. The theoretical models are written as a sum of paths of the photoelectron. A path is the contribution to the EXAFS data by a component of the photoelectron that travels from the absorbing atom and then is scattered from one or more neighboring atoms and finally returns to the absorbing atom. Each path has several adjustable parameters optimized by FEFFIT to fit the data. These parameters include the passive electron reduction factor (S_0^2), the number of identical paths (N_{degen}), the relative mean-square displacement (Debye-Waller factor) of the atoms included in path i (σ_i^2), an energy shift for each path (ΔE_{0i}), and a change in the path length with respect to crystallographic values (Δr_i). Several of our models include as many as 4 paths, and therefore, several constraints were used to reduce the number of fit parameters. These constraints are discussed in detail in the section that describes each model.

S_0^2 N_{degen} and S_0^2 are both constant multiplication factors in the EXAFS theory used to construct the models, as in equation 7.1. Therefore, only the product $N_{degen}S_0^2$ can be determined. In K-edge data from an InAs standard sample were collected to decouple these constants. The crystallographic structure of InAs is known, so N_{degen} is no longer a fitted parameter. Thus the value for S_0^2 of 1.0428 ± 0.0283 was determined by the simulation of the EXAFS data from the InAs standard sample taken in transmission mode.

Debye-Waller Factor According to the correlated Debye and Einstein models of Mean Square Relative Displacement(MSRD) [114, 115], MSRD between absorber and back scattering atoms is inversely proportional to the effective mass of the 2-atom system:

$$M = \frac{M_1 M_2}{M_1 + M_2}\,. \tag{7.7}$$

In equation 7.7, M_1, M_2 are the atomic mass of the 2 atoms respectively, while M is the effective mass of the 2-atom system.
In the simulation, the Debye-Waller factors for In-Sb, In-N bonds were set based on the Debye-Waller factor of the In-As bond according to equation (7.7).

7.5.2 Model and Result

The Fourier transform of the In K-edge data from sample R15 is shown in Fig. 7.6. The spectrum shows clearly the peak corresponding to the first coordination shell. Peaks corresponding to the second and third shells were not observable in the spectrum, possibly because of the complex structure of the quinary alloy. The dashed lines represent

Atomic type	Δr	σ_i^2	concentration
In→As	Δr_1	σ_1^2	1-y
In→Sb	Δr_3	$\sigma_1^2 \times 0.767$	y

Table 7.1: Parameters used to describe the model for In K-edge data from the samples, with 2 paths for In-As and In-Sb.

Atomic type	Δr	σ_i^2	concentration
In→As	Δr_1	σ_1^2	1-x-y
In→Sb	Δr_3	$\sigma_1^2 \times 0.767$	y
In→N	Δr_2	$\sigma_1^2 \times 3.63$	x

Table 7.2: Parameters used to describe the model for In K-edge data from the samples, with 3 paths for In-As, In-Sb, and In-N.

the fitting range of the first coordination shell (R from 1.589 to 2.708 Å). The fitting range in k space was 4.247-14.936 $Å^{-1}$.

A trial structure is given as input to the FEF7 code to generate a theoretical model. The theoretical models consisted of 3 paths: In-As, In-Sb, and In-N paths. In each path, there are 3 parameters to be adjusted to optimize FEFIT to fit the data, which are S_0^2, σ_i^2 (D-W factor of each path), and Δr_i. The variables used in the model are listed in Table 7.1 and Table 7.2.

The spectrum was first simulated with a model constructed with 2 paths: In-As and In-Sb. In the simulation, Δr_3 was set to 0. σ_3^2 was set to $0.767 \times \sigma_1^2$ for the reasons explained in section 7.5.1 (Table 7.1). The amplitude of the In-As path was reduced by weighting with (1-y) and the In-Sb path amplitude was increased by weighting with y to account for the contribution of Sb atoms to the backscattering of the first shell.

In the model, the In-As distances were set to be the same as in the tetrahedral binary compounds [116], which was tested by fitting the EXAFS of our standard samples(2.6233 Å). The In-Sb distance was varied within values less than the bond length of the binary compound, 2.8057 Å [117], from 2.7063 to 2.8055 Å. The assumption of this construction of the trial structure is that in the main skeleton of the INGAS crystal, the main atomic bonds remain approximately the same as in the corresponding binary compounds [118]. The incorporation of dilute Sb and N forms bonds with In of varying lengths. The proportion of Sb atoms in the In neighborhood (y) was varied from 0.01 to 0.1. The value of S_0^2 was set as 1.0428 (Section 7.5.1). An overall edge energy shift $\Delta E0$ was determined in the simulation. The data and fit range resulted in 5.38 independent points (In FeFFIT, the number of independent points was calculated as $N_{idp} = 2\Delta k \Delta R/\pi$, where Δk and ΔR are the grid spacing in K- and R-space). Varying both the In-Sb distances and Sb concentration y, we constructed 70 trial structures and tested their ability to reproduce the EXAFS experimental data.

Subsequently, we fit the R15 spectrum with a trial structure composed of 3 paths: In-As, In-Sb and In-N. The variables used in the model are listed in Table 7.3. In the fitting, Δr_2 and Δr_3 were set to 0, and the length of the In-Sb bond used in the fitting was the value with minimum RCS from the 2 path fitting (In-Sb distance of 2.741 Åand

Atomic type	Δr	σ_i^2	concentration
In→As	Δr_1	σ_1^2	1-x-y-z
In→Sb	Δr_3	$\sigma_1^2 \times 0.767$	y
In→N	Δr_2	$\sigma_1^2 \times 3.63$	x
In→complex	Δr_4	$\sigma_1^2 \times ratio$	z

Table 7.3: Parameters used to describe the model for In K-edge data for the samples, with 4 paths. The ratio is calculated as discussed in Section 7.5.1, based on the atomic mass.

Mass (atomic unit)	28	73	101	108	122	133	158	209
In-complex distance (Å)	2.08	2.08	2.04	2.04	2.04	2.04	2.04	2.04
First shell fraction	0.02	0.01	0.02	0.02	0.02	0.02	0.02	0.02
RCS	1.01	1.37	0.76	0.512	0.346	0.76	0.96	2.16

Table 7.4: Minimum RCS values resulted with different complex masses in the 4-paths simulation, the corresponding In-complex distances and complex first shell fraction in the models.

Sb fraction (y) of 0.02). The value of S_0^2 was set to 1.0428 (Section 7.5.1). The overall energy shift ΔE_0 was determined in the simulation. The data and fit range resulted in 5.38 independent points. The In-N distance was varied around the bond length in binary InN compounds, 2.1356 Å [119], from 2.0785 to 2.3816 Å. The result of the best fit with the 3-path model is shown in Fig. 7.7.

After the fitting with 2 and 3 paths with varying In-Sb and In-N distances and Sb, N concentrations y and x, we found the RCS resulting from these fits to lie close to each other. No one trial model is obviously better than the others. Upon fitting with In-Sb distances from 2.7063 Åto 2.8055 Åand Sb concentrations from 0 to 10%, the RCS values of 62 out of the 71 resulting models are within 1-sigma error. The addition of an In-N path in the trial model resulted in increased RCS values, in the range of In-N distances of 2.0785 Åto 2.3816 Åand N atom concentrations of 0.5% to 12%.

At the same time, there is a shoulder on the small R side of the first coordination shell peak that cannot be reproduced with these models. Since the INGAS samples were grown under non-equilibrium conditions, there are generally structural defects within the samples. According to a previous study by other techniques on dilute nitride alloys, there are several forms of complex defects possibly existing in the alloy [120,121]. We suppose this shoulder at the low R side of the first shell peak (S_1) is due to a structural complex at a distance somewhat smaller than the first shell distance.

In order to mimic the possible complex responsible for this feature in the spectra, we constructed models with a 4th path composed of atoms with different atomic masses and distances from the In atom, and tested their ability to reproduce the spectra.

Table 7.4 lists the minimum RCS values obtained for each particle mass and the distance of the particle from In atoms. The simulation shows a much reduced RCS value for particles with mass of 122±20 atomic unit. The minimum RCS value was obtained for the particle with a mass of 122 (RCS = 0.346). The RCS of this fit is more than 1-sigma error lower than those of the models constructed with only 3 paths. This indicates that the S_1-related complex structure has a mass close to 122 with the In-complex

distance of 2.0352 Åand a complex fraction of 2 %. The simulation result obtained with this 4-path model is displayed in Fig. 7.8.

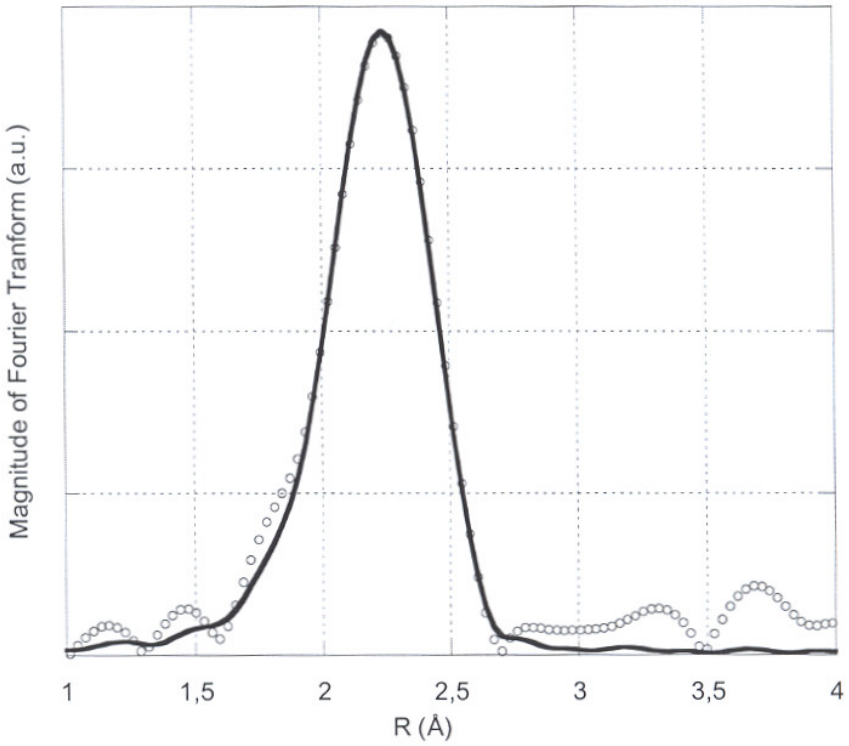

Figure 7.7: Magnitude of the Fourier transform of the In K-edge data of sample R15: Experimental data (dots) and fits with a 3-path model (continuous line)

Considering that the low-R side shoulder might be caused by noise on the high k values (Section 7.4.2), we tried changing the fitting range of k, with a lower maximum value of 13.328 $Å^{-1}$. The resulting change of RCS is in agreement with the fit result for k of 4.247 to 14.936 $Å^{-1}$, as shown in Figs. 7.9 and 7.10. The fit with 4 paths resulted in an RCS value about 1.08 smaller than that for 3 paths.

To further test this assumption, we applied the same simulation procedures to the other two samples. The fitting range of the first coordination shell was 1.676-2.689 Åfor A0 and 1.751-2.692 Åfor A3. The fitting ranges in k space for the spectra of A0 and A3 are 3.902-14.938 $Å^{-1}$ and 3.964-13.523 $Å^{-1}$, respectively. Similar results were obtained in the simulation of these 2 samples. In the simulation with 2 paths of the data from sample A0, RCS values for 64 out of the 71 models are within 1-sigma error. In the 3-path simulation, 42 out of 55 of the RCS values are within 1-sigma error. For sample A3, with a 2-path simulation, 53 out of 71 RCS values are within 1-sigma error. In the 3-path simulation, 68 out of 78 RCS values are within 1-sigma error. The best fits with a 3-path model and with a 4-path model obtained for A0 are shown in Fig. 7.11 and Fig. 7.12, respectively. The best fitting results for sample A3 with the two types of models are displayed in Figs. 7.13 and 7.14.

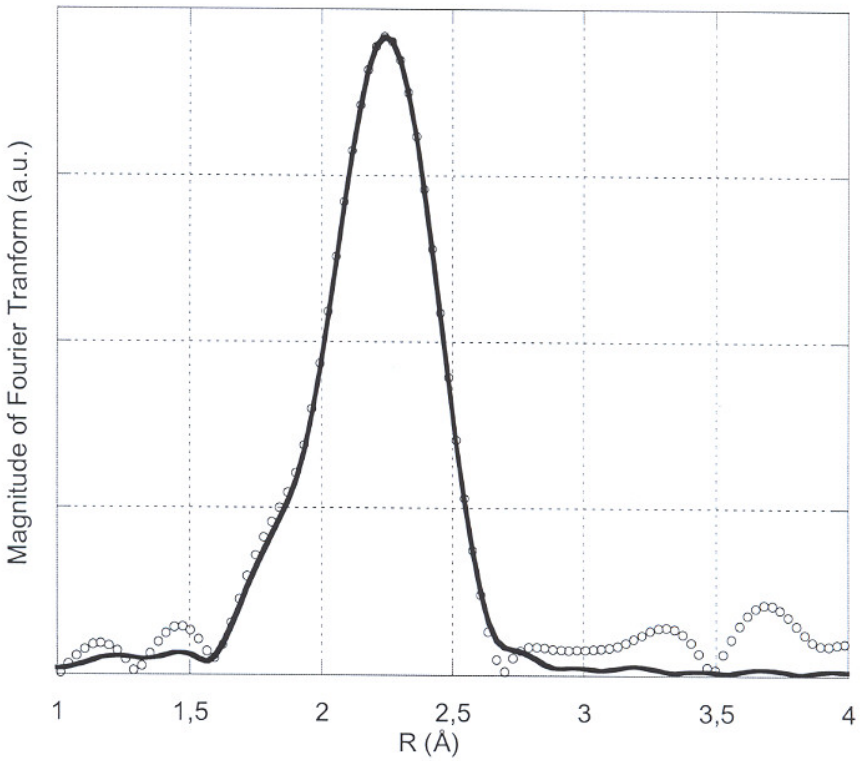

Figure 7.8: Magnitude of the Fourier transform of the In K-edge data of sample R15: Experimental data (dots) and fits with a 4-path model (continuous line)

7.5.3 Possible N-related Complex Structure

Since the first shell fraction of the S_1-related structural complex is much higher than the ordinary contamination-related defects and its concentration increases after annealing with longer durations, combined with the consideration that the samples were grown by solid-state MBE, we suppose that this structural complex is not caused by impurities.

One possibility is that it is due to Sb atoms at around 2.04 Åfrom In atoms. But in fact the Sb atom is too large to remain at such a close position from the In atom, thus this unstable configuration should relax and be annihilated upon annealing. on the contrary, our experimental results revealed that the concentration of the S_1-related structure complex increased after an annealing process (data shown later in Fig. 7.15).

Moreover, we found that the mass of 122 atomic unit is also close to the sum of the masses of one N-N dimer and a N-As pair. We also noticed that although with a mass far from 122, the model with particle mass of 28 also resulted in an RCS value within 1-sigma error (Table 7.4). This means the model could reveal the complex structure with an acceptable accuracy. In fact, the mass of 28 is the same as that of a N-N dimmer. Therefore, we believe that the S_1-related complex is composed of a N-N dimer and a N-As pair. In fact,$(\text{N-N})_{As}$ and $(\text{N-As})_{As}$ defects have been observed in dilute nitride alloys several times to date [120–124]. This study revealed that these defects may exist at a much shorter distance from the In atoms, i.e., they exist at the interstitial positions

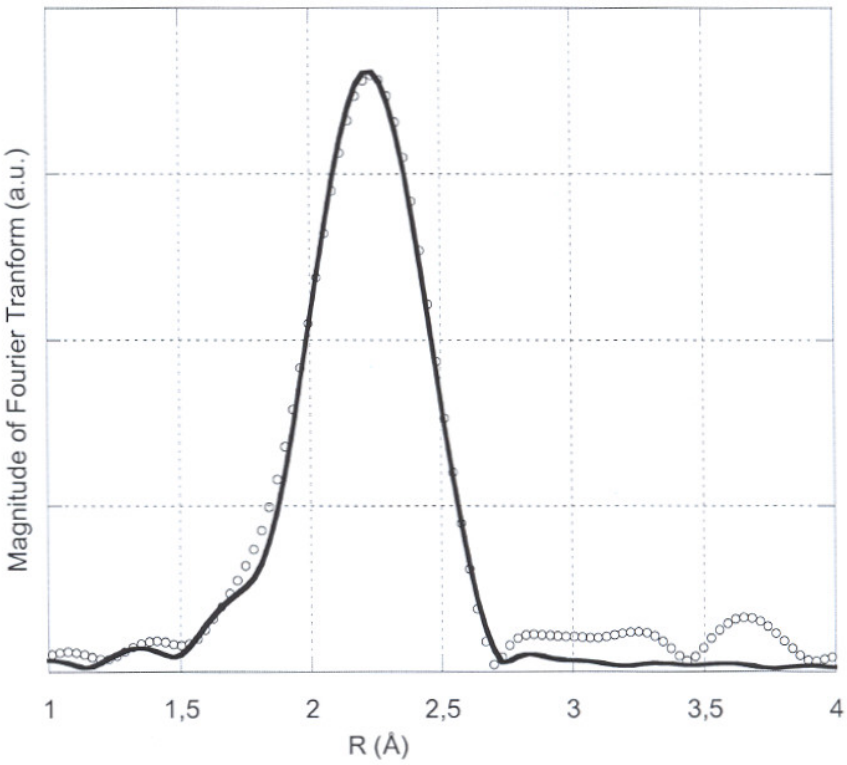

Figure 7.9: Magnitude of the Fourier transform of the In K-edge data of sample R15, with a k range of 4.247-13.328 $Å^{-1}$: Experimental data (dots) and fits with a 3-path model (continuous line).

rather than occupying a lattice site [125].

7.5.4 Change of N-related Complex Structures upon Annealing

The different In-complex distances and In first shell fractions of the complex structure in the 3 samples were displayed in Fig. 7.15. The error bars were determined by the RCS values resulting from those models within 1-sigma-error. The complex mass was set at 122 atomic units in the fitting. Upon annealing for 15 s, the sample shows a shorter In-complex distance and a tendency of lower complex fraction; the sample after annealing for 60 s shows the largest In-complex distance and the tendency of highest complex fraction.

According to the first principle calculation of Zhang *et al.* [121], the $(N\text{-}As)_{As}$ structure has a much higher defect formation energy than that of N-N split interstitial and can survive high T annealing. Thus the $((N\text{-}As)_{As}$ defects are believed to be stable defects.

We believe that in the as-grown sample, there are N-N and N-As pair defects formed at a distance of about 2.04 Åfrom In atoms. Upon annealing for 15 s, part of the defects were annihilated. This results in a decrease of the complex concentration and a small decrease in the In-complex distance. During annealing of 60 s, part of the N atoms separated from the N-N dimers, combined with As atoms, and formed additional N-As interstitial defects. This caused the increase of the complex portion in the first shell

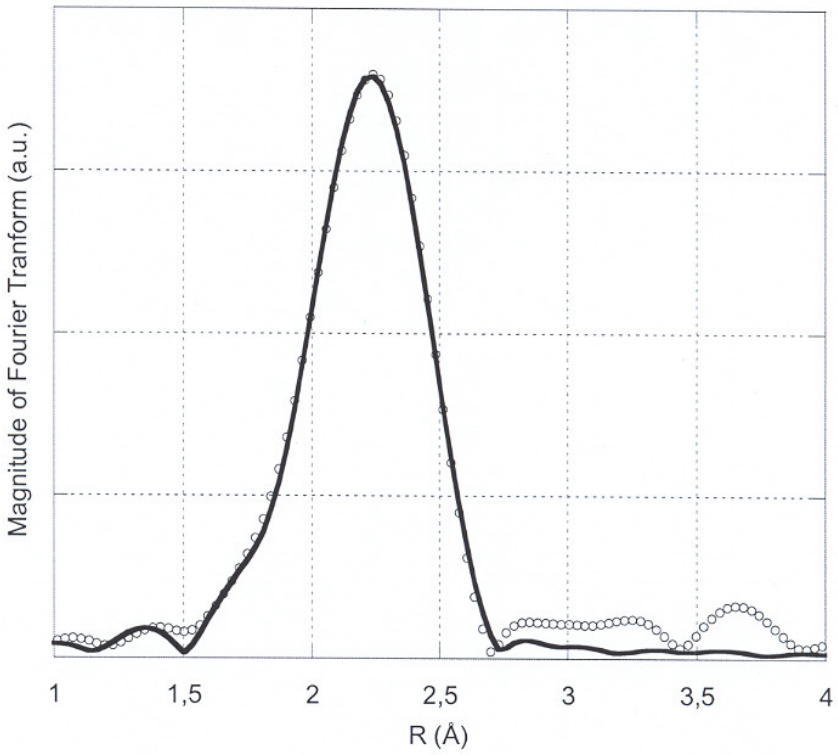

Figure 7.10: Magnitude of the Fourier transform of the In K-edge data of sample R15, with a k range of 4.247-13.328 $Å^{-1}$: Experimental data (dots) and fits with a 4-path model (continuous line).

and the increase of the In-complex distance, since the As-N defects exist at a larger distance because of the structural relaxation and/or larger atomic radii of the As atoms. A similar phenomenon was observed by Dhar *et al.* [124] in their photocapacitance measurements on GaAsN layers.

In the PL measurement (data not shown here), sample R15 showed the highest emission intensity among the 3 samples under study. This is consistent with the results that the first-shell fraction of the complex is highest in sample R15 in the EXAFS study.

It should be noted that this study has examined only different particle masses. Other factors that affect the absorption cross section, such as the backscattering function, should also be considered in further work.

7.5.5 Sb and N Atomic Fractions in the In First-Neighbor Shell

With a 4-path model, we also explored the Sb, N atomic fractions in the near neighborhood of In for the three samples respectively. The Sb fraction is in the range of 0-4%, and the N fraction is in the range of 0-11% for the 3 samples. The Sb and N first-shell fraction did not show a distinguishable difference within 1-sigma-error range among the 3 samples investigated. Thus, we cannot decide directly whether there is a preferential bonding pair between any 2 elements in the quinary alloy in this study [126–128].

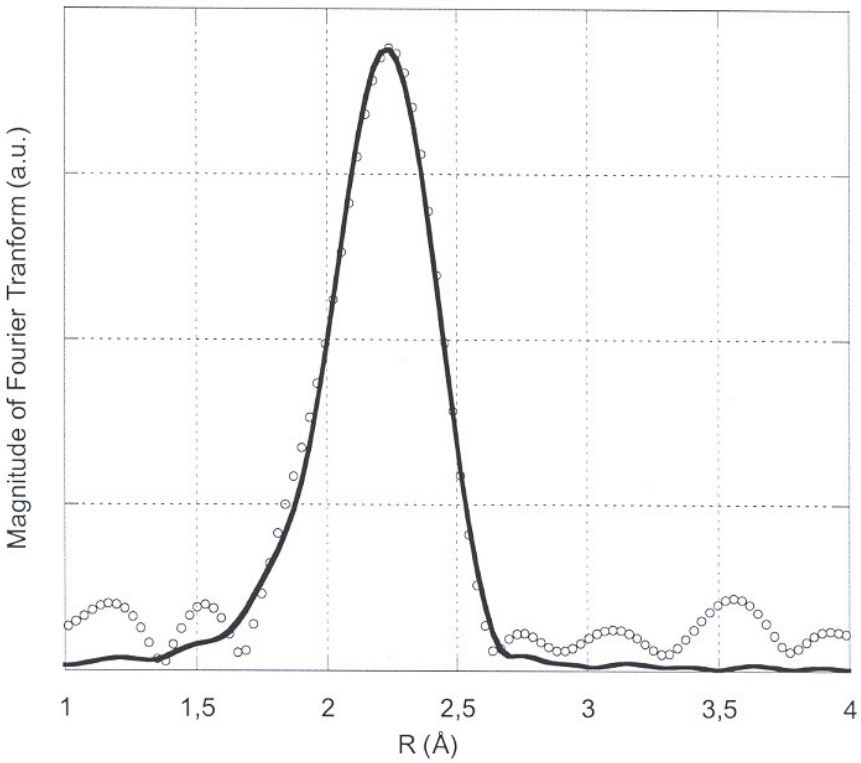

Figure 7.11: Magnitude of the Fourier transform of the In K-edge data of sample A0: Experimental data (dots) and fits with a 3-path model (continuous line).

Summary We investigated the In first-shell neighborhood atomic structures of InGaAsSbN MQWs (as grown, annealed at 800°C for 15 s and 60 s respectively) by analyzing the In K-edge EXAFS oscillations.

The Sb and N fractions in the first shell were determined to be in the range of 0-4% and 0-11% respectively by the EXAFS study.

In addition, there is a defect complex related feature in the EXAFS spectra. The possible structure of this complex is proposed to be combined N-N pair and N-As pair defects, at a distance of around 2.04 Åfrom the In atom. After annealing of 15 s, part of the defects were annihilated, resulting in a decrease of the complex fraction in the In first shell and a tiny reduction of its distance from In atoms. Upon annealing for 60 s, part of the N-N defects convert to N-As defects, leading to an increase in their concentration and distance from the In atoms.

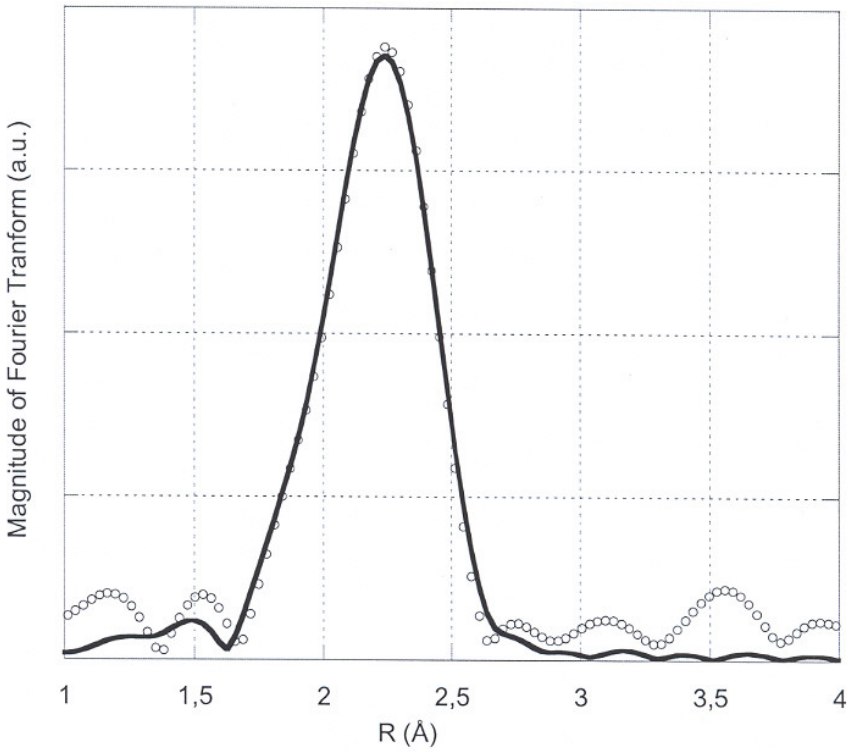

Figure 7.12: Magnitude of the Fourier transform of the In K-edge data of sample A0: Experimental data (dots) and fits with a 4-path model (continuous line).

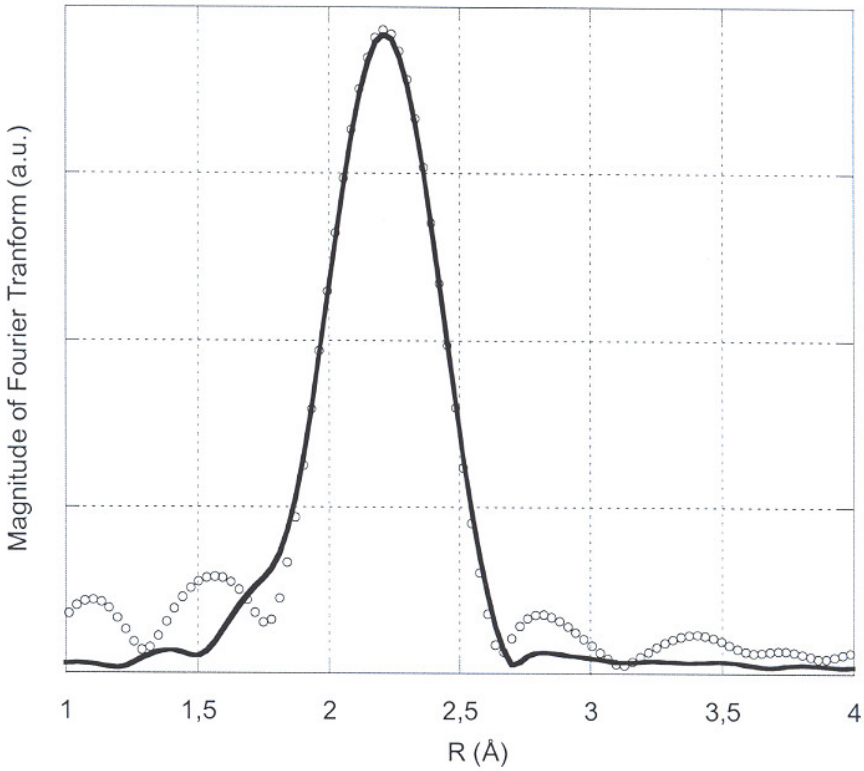

Figure 7.13: Magnitude of the Fourier transform of the In K-edge data of sample A3: Experimental data (dots) and fits with a 3-path model (continuous line).

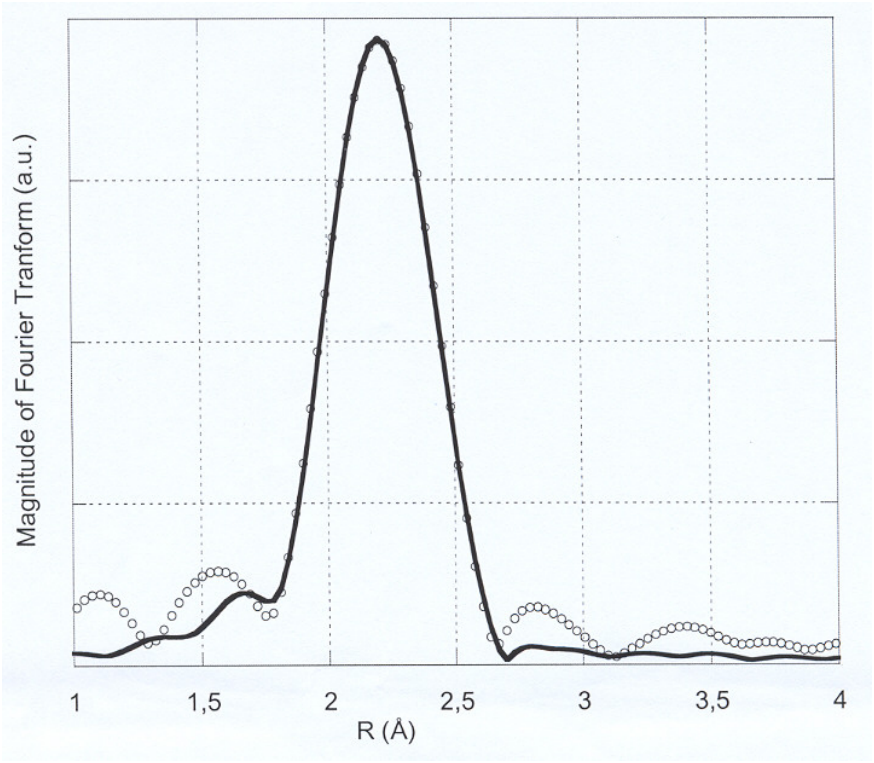

Figure 7.14: Magnitude of the Fourier transform of the In K-edge data of sample A3: Experimental data (dots) and fits with a 4-path model (continuous line).

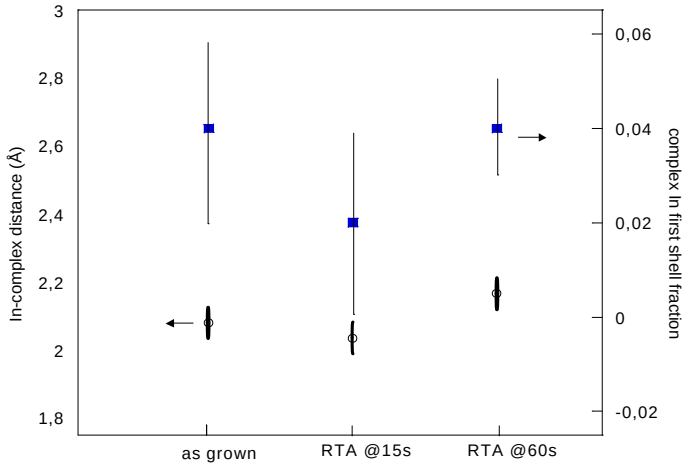

Figure 7.15: The In complex distances and the complex structure fraction in the first shell of In atoms obtained by simulation for sample A0, R15 and A3.